Lineage-specific and single-cell chromatin accessibility charts human hematopoiesis and leukemia evolution

M Ryan Corces[1–3,11], Jason D Buenrostro[3–5,11,12], Beijing Wu[4], Peyton G Greenside[4,6], Steven M Chan[7], Julie L Koenig[1,2], Michael P Snyder[3,4], Jonathan K Pritchard[4,8,9], Anshul Kundaje[4,10], William J Greenleaf[3,4], Ravindra Majeti[1,2,12] & Howard Y Chang[3,12]

We define the chromatin accessibility and transcriptional landscapes in 13 human primary blood cell types that span the hematopoietic hierarchy. Exploiting the finding that the enhancer landscape better reflects cell identity than mRNA levels, we enable 'enhancer cytometry' for enumeration of pure cell types from complex populations. We identify regulators governing hematopoietic differentiation and further show the lineage ontogeny of genetic elements linked to diverse human diseases. In acute myeloid leukemia (AML), chromatin accessibility uncovers unique regulatory evolution in cancer cells with a progressively increasing mutation burden. Single AML cells exhibit distinctive mixed regulome profiles corresponding to disparate developmental stages. A method to account for this regulatory heterogeneity identified cancer-specific deviations and implicated HOX factors as key regulators of preleukemic hematopoietic stem cell characteristics. Thus, regulome dynamics can provide diverse insights into hematopoietic development and disease.

The human hematopoietic system is maintained by a small number of self-renewing multipotent hematopoietic stem cells (HSCs). More than 200 billion blood cells are produced in a single day[1], highlighting the need for exquisite regulation that balances self-renewal of upstream stem cells with downstream production of differentiated effector cells. Previous studies have profiled gene expression patterns in mouse[2,3] and human[4,5] hematopoiesis, providing a rich resource for characterizing these cellular states. However, measuring gene expression alone provides limited information regarding regulators of cell identity. Alternatively, genome-wide chromatin-based assays are sensitive methods for assessing the activity of *trans*-acting factors and *cis*-regulatory elements. Recently, several methods have been developed to profile the epigenomes of rare cellular populations[3,6,7], enabling the identification of regulatory elements in mouse hematopoiesis[3]. These methods have not yet been used to profile epigenomes for rare progenitor populations in human hematopoiesis.

Dysregulation of the regulatory networks governing the human hematopoietic system has a critical role in the development of hematological malignancies[8]. The long lifespan of HSCs makes them susceptible to the accumulation of mutations over time[9,10]. In particular, in the case of AML, HSCs isolated from patients with leukemia have been shown to harbor some but not all of the genetic alterations found in leukemic cells. These cells, termed preleukemic HSCs[11–13],

provide insight into the earliest stages of dysregulation of normal hematopoiesis leading to AML.

We previously described an assay for transposase-accessible chromatin using sequencing (ATAC-seq), a method capable of measuring chromatin accessibility in rare cellular populations[6]. Here we report the development of an improved ATAC-seq protocol, optimized for human blood cells, that allows for more rapid high-quality measurements. We apply this optimized protocol to cells isolated from 9 healthy human donors and 12 patients with AML, studying a total of 137 samples representing 16 of the major cell types of the normal hematopoietic and leukemic hierarchies. In addition, we measure the transcriptomes of 96 samples from the same healthy and leukemic donors to derive paired expression data. This reference map highlighted the effects of both early mutations in epigenetic modifiers and late mutations in proliferation-inducing oncogenes on the leukemogenic process. Our results provide key insights into the evolutionary process of leukemogenesis and identify important regulatory programs that could be targeted to disrupt this process during its earliest stages.

RESULTS

Fast-ATAC is an optimized ATAC-seq protocol for blood cells

We created a reference regulome and transcriptome map of the normal hematopoietic hierarchy (**Fig. 1a,b**). We developed an

---

[1]Institute for Stem Cell Biology and Regenerative Medicine, Stanford University School of Medicine, Stanford, California, USA. [2]Division of Hematology, Department of Medicine, Stanford University School of Medicine, Stanford, California, USA. [3]Center for Personal Dynamic Regulomes, Stanford University School of Medicine, Stanford, California, USA. [4]Department of Genetics, Stanford University, Stanford, California, USA. [5]Broad Institute of MIT and Harvard, Harvard University, Cambridge, Massachusetts, USA. [6]Program in Biomedical Informatics, Stanford University School of Medicine, Stanford, California, USA. [7]Princess Margaret Cancer Centre, University Health Network, Toronto, Ontario, Canada. [8]Department of Biology, Stanford University, Stanford, California, USA. [9]Howard Hughes Medical Institute, Chevy Chase, Maryland, USA. [10]Department of Computer Science, Stanford University, Stanford, California, USA. [11]These authors contributed equally to this work. [12]These authors jointly directed this work. Correspondence should be addressed to R.M. (rmajeti@stanford.edu) or H.Y.C. (howchang@stanford.edu).

optimized protocol for use on primary blood cells, termed Fast-ATAC, which relies on a one-step membrane permeabilization and transposition using the lysis reagent digitonin. We found that this simplified protocol requires just 5,000 cells, provides high-quality data with reduced noise (**Supplementary Fig. 1a–c**), reduces the frequency of mitochondrial reads by ~5-fold (**Supplementary**

Fig. 1d), and offers an approximately 5-fold improvement in fragment yield per cell (**Supplementary Fig. 1e**).

Using Fast-ATAC and RNA-seq, we profiled the chromatin accessibility landscapes (regulomes) and transcriptomes of 13 distinct cellular populations from the human hematopoietic hierarchy isolated via FACS (**Fig. 1a** and **Supplementary Figs. 2–4**). Cells were
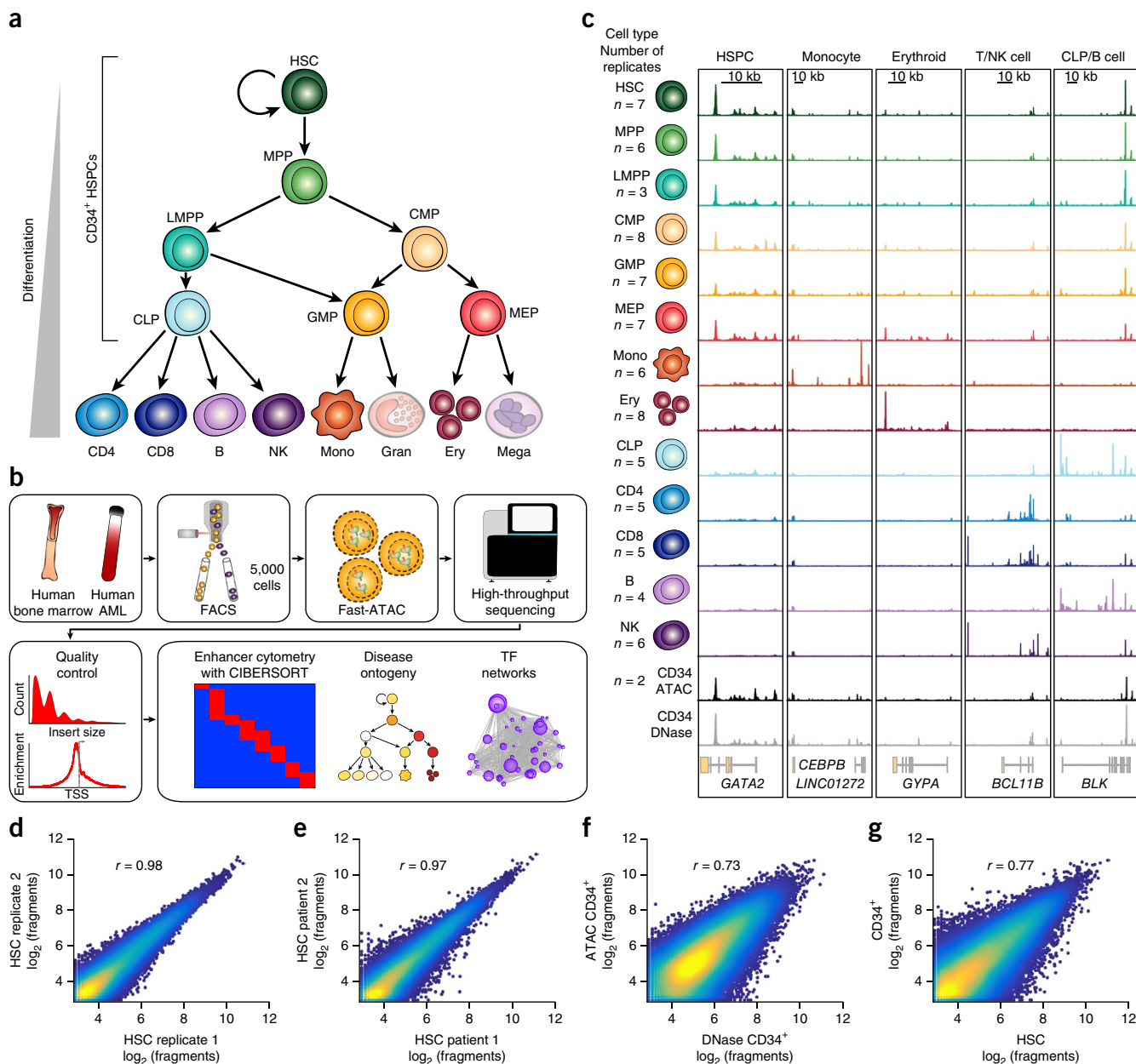

Figure 1 Interrogation of chromatin landscapes in primary blood cells. (**a**) Schematic of the human hematopoietic hierarchy showing the 13 primary cell types analyzed in this work. Granulocytes and megakaryocytes were excluded. The cell types comprising CD34+ HSPCs are indicated. Colors used in this schematic are consistent throughout the figures. Mono, monocyte; gran, granulocyte; ery, erythroid; mega, megakaryocyte; CD4, CD4+ T cell; CD8, CD8+ T cell; B, B cell; NK, natural killer cell. (**b**) Diagram of the analyses performed using paired ATAC-seq and RNA-seq data in both primary human blood cells and primary patient-derived AML cells. (**c**) Normalized ATAC-seq profiles at developmentally important genes. Profiles represent the union of all technical and biological replicates for each cell type. See **Supplementary Table 1** for the exact number of technical and biological replicates for each cell type. Genomic coordinates for the loci: *GATA2*, chr. 3: 128,197,777–128,218,433; *CEBPB*, chr. 20: 48,800,260–48,904,715; *GYPA*, chr. 4: 145,020,689–145,070,000; *BCL11B*, chr. 14: 99,513,898–99,796,947; *BLK*, chr. 8: 11,343,117–11,429,285. All y-axis scales range from 0–10 in normalized arbitrary units. The x-axis scale is indicated by the scale bars. (**d–g**) Scatterplots showing correlation of technical replicates (**d**), different human donors (**e**), ATAC-seq and DNase-seq data derived from CD34+ HSPCs (**f**), and ATAC-seq data for HSCs and bulk CD34+ HSPCs (**g**). The r values reported were calculated from correlation of all peaks. Plots show 50,000 random peaks, each with at least five reads.

taken directly from donor bone marrow or peripheral blood without further manipulation (**Supplementary Table 1**). The cell populations isolated included seven unique stem and progenitor and six differentiated cell types spanning the myeloid, erythroid, and lymphoid lineages[14–17]. Altogether, we performed ATAC-seq and RNA-seq on 3–4 adult donors for each cell population, generating a total of 49 transcriptomes and 77 regulomes (**Fig. 1c**, **Supplementary Figs. 1f and 5a,b**, and **Supplementary Table 1**).

With this data set, we identified a total of 590,650 accessible peaks. We found Fast-ATAC profiles to be highly reproducible across technical ($r = 0.98$; **Fig. 1d**) and biological ($r = 0.97$; **Fig. 1e**) replicates in HSCs. In addition, we found similarly high concordance across all other cell types for all technical and biological replicates (mean $r = 0.94$ and 0.91, respectively; **Supplementary Fig. 1g,h**), except for erythroblast cells (technical replicates, $r = 0.55$; biological replicates, $r = 0.50$). Each individual cell type of the hematopoietic hierarchy displayed a set of uniquely expressed genes and uniquely accessible chromatin regions mapping to genes known to be involved in cellular functions important for the given cell type (**Fig. 1c** and **Supplementary Fig. 6a–c**).

We also observed reasonable correlation ($r = 0.73$) between Fast-ATAC and DNase-seq[18] results for CD34+ hematopoietic stem and progenitor cells (HSPCs) (**Fig. 1f**). Notably, we found that HSCs, a CD34+ subpopulation, could have different ATAC-seq profiles

than the bulk CD34+ HSPC pool ($r = 0.77$ observed versus $r = 0.91$ expected for replicates of the same cell type; **Fig. 1g**), highlighting the value of highly purified stem and progenitor cell subpopulations for epigenomic analysis.

Distal element accessibility is highly cell type specific

Unsupervised hierarchical clustering of our RNA-seq and ATAC-seq data showed robust classification of cell types among technical and biological replicates (**Fig. 2a–d** and **Supplementary Fig. 7a–d**). In this analysis, we observed that chromatin accessibility was more adept than mRNA expression levels at classifying cell types, as quantified by cluster purity[19], suggesting that chromatin accessibility is more cell type specific and better captures cell identity. However, we note that RNA information from enhancer transcription, splicing, or other features that require optimized methods and deeper sequencing may improve cell type classification. When regulatory elements were subdivided as gene promoters or distal elements (>1,000 bp away from a transcription start site (TSS)), we found that distal elements provided significantly improved cell type classification in comparison to promoters (**Fig. 2e,f**), similar to previous observations using DNase-seq and ChIP-seq data[20,21]. This observation is clearly illustrated by the region surrounding the *TET2* gene. Despite the invariant expression of *TET2* and ubiquitous accessibility of the *TET2* promoter, we found highly diverse accessibility profiles within
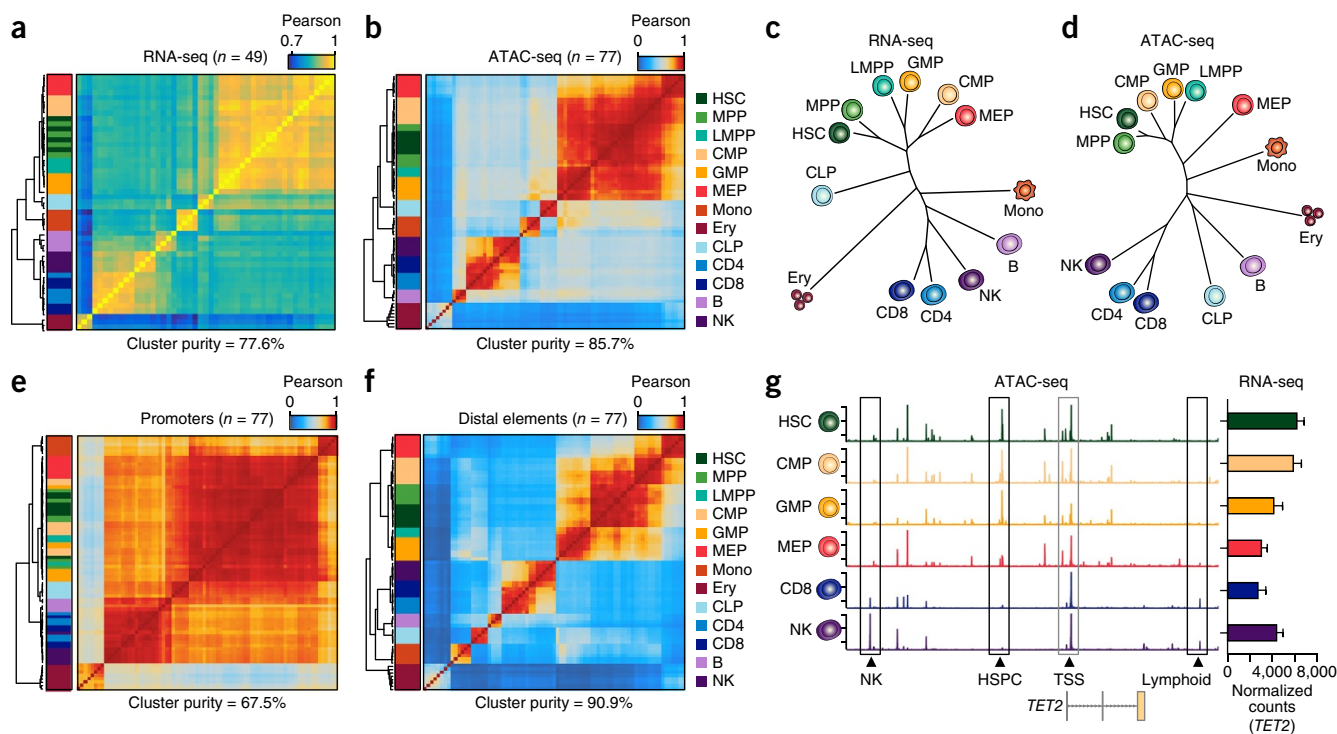

Figure 2 Distal regulatory elements enable accurate classification of the hematopoietic hierarchy. (**a,b**) Unsupervised hierarchical clustering of RNA-seq (**a**) and ATAC-seq (**b**) data from all replicates of 13 normal hematopoietic cell types. Values shown are Pearson correlation coefficients. Cluster purity quantifies the degree that cells of the same lineage are clustered together. For RNA-seq, clustering was performed using variance-stabilizing transform–normalized expression data for all expressed annotated genes. For ATAC-seq, clustering was performed on all peaks using quantile-normalized quantitative read coverage data. (**c,d**) Phylogenetic dendrograms of RNA-seq (**c**) and ATAC-seq (**d**) data showing correlations between cell types. Length of tree branches represents Euclidean distance. Data represent the union of all technical and biological replicates for each cell type. (**e,f**) Hierarchical clustering of ATAC-seq profiles mapping to promoters (**e**) and distal regulatory elements (**f**). Values shown are Pearson correlation coefficients. Promoter-proximal peaks are defined as peaks within 1 kb of an annotated TSS. Distal element peaks are defined as peaks greater than 1 kb from an annotated TSS. (**g**) ATAC-seq peaks in the *TET2* locus show highly variable distal regulatory landscapes (left) and relatively constitutive expression of *TET2* (right). Data represent the union of all technical and biological replicates for each cell type: HSC, 7; CMP, 8; GMP, 7; MEP, 7; CD8, 5; NK, 6. Error bars, 1 s.d. Genomic coordinates: chr. 4: 106,031,731–106,073,198. The y-axis scales range from 0–10 in normalized arbitrary units. Boxed regions show cell-type-specific or constitutive peaks around the *TET2* gene.

nearby distal regulatory elements, clearly distinguishing HSPCs, natural killer (NK) cells, and T cells (**Fig. 2g**).

Enhancer cytometry deconvolves complex cell populations

Given the accuracy with which distal regulatory landscapes delineate cell types, we hypothesized that Fast-ATAC data can be used to deconvolve highly complex cellular populations, such as CD34+ HSPCs, into their constitutive subsets (**Fig. 3a**). The highly cell-type-specific nature of our ATAC-seq data enabled the development of a strategy we term 'enhancer cytometry', wherein we enumerate the frequency of cell types in complex cellular mixtures *in silico* on the basis of chromatin accessibility data. To do this, we employ the deconvolution algorithm CIBERSORT[22] to quantify the contribution of each individual cell type to the ensemble profile (Online Methods). Using a filtered peak list, we applied CIBERSORT to define a set of cell-type-specific regulatory elements (**Fig. 3b** and **Supplementary Table 2**). We validated this approach using leave-one-out cross-validation and found that enhancer cytometry was able to classify all normal hematopoietic cell types (**Fig. 3c,d** and **Supplementary Fig. 8a–g**). One exception was the discrimination of HSCs and multipotent progenitor cells (MPPs), which have similar epigenomic profiles and therefore showed reasonable but lower accuracy than other cell types (**Supplementary Fig. 8a,g**). Comparison of enhancer cytometry on bulk CD34+ HSPCs to ground truth flow cytometry data showed accurate enumeration of the constituent cell types ($r^2 = 0.95$; **Fig. 3e,f**). Notably, cell type deconvolution of CD34+

HSPCs using all regulatory elements, including promoters, was not as accurate ($r^2 = 0.91$; **Supplementary Fig. 8h**). In addition, we found that enhancer cytometry could also be used to deconvolve CD34+ DNase-seq data (**Supplementary Fig. 8i**), suggesting that ATAC-seq with enhancer cytometry may be a general strategy for identifying and enumerating cell types within existing epigenomic data from complex cellular mixtures.

Regulatory networks of normal hematopoiesis

To better understand the mechanisms governing these diverse regulatory landscapes, we sought to quantify the effect of specific *trans*-acting factors at each developmental transition. We adapted a computational framework to measure gain or loss of accessibility across regulatory elements sharing a feature or annotation, for example, a transcription factor motif (Online Methods)[23]. For subsequent visualization, we clustered similar motifs to create a non-redundant list we call 'hematopoiesis transcription factor motifs' ($n = 46$; **Fig. 4a** and Online Methods). We found transcription factor motifs such as GATA, RUNX, and SPI1 to be dominant regulators of chromatin accessibility, consistent with published results[24–26] (**Fig. 4a** and **Supplementary Fig. 9a**). We found that activation of these transcription factors was cell type specific, often displaying stepwise gains across developmental lineages (**Supplementary Table 3**). This is exemplified by the GATA and PAX motifs, which were strongly enriched in erythroid and lymphoid lineages, respectively (**Fig. 4b,c**). To validate this approach for determining global transcription factor motif regulators of cell
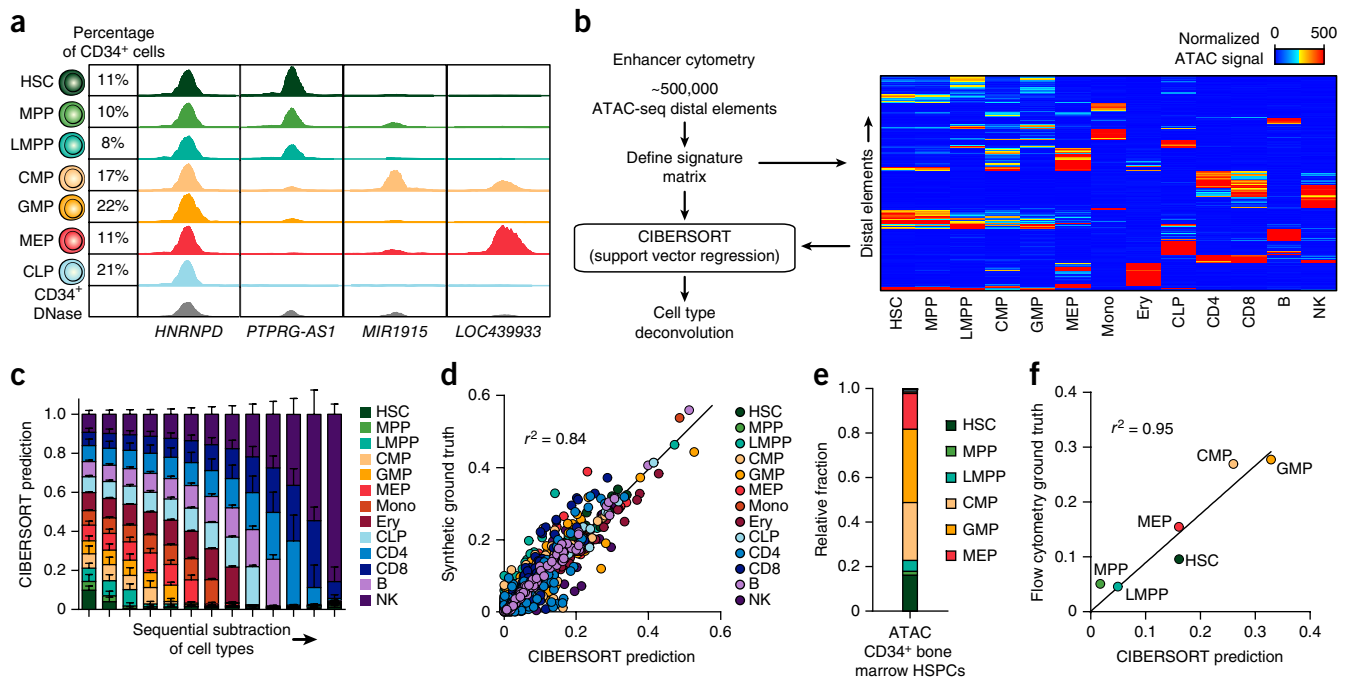

Figure 3 Enhancer cytometry allows for deconvolution of the hematopoietic hierarchy. (**a**) Normalized ATAC-seq profiles of HSPC subsets and ensemble CD34+ HSPC DNase-seq profiles illustrating heterogeneity among CD34+ HSPC subpopulations. Predicted cell fractions based on flow cytometry of six healthy bone marrow donors are shown on the left, and the nearest annotated genes are shown below. Genomic coordinates: *PTPRG-AS1*, chr. 3: 62,194,000–62,196,000; *LOC439933*, chr. 4: 35,761,750–35,763,750; *MIR1915*, chr. 10: 21,639,750–21,641,750; *HNRNPD*, chr. 4: 83,205,250–83,207,250. The *y*-axis scales range from 0–10 in normalized arbitrary units. (**b**) Schematic of enhancer cytometry with cell-type-specific distal elements ($n = 735$; right). The signature matrix heat map has an upper bound of 500, and all elements with signal greater than 500 appear red. (**c,d**) Benchmarking of enhancer cytometry using randomly permuted synthetic mixtures to test robustness to sequential subtraction (**c**) and randomized mixture content (**d**). Test data and training data are non-overlapping. In **c**, synthesized 'ground truths' following subtraction are equal mixtures of the remaining cell types. In the leftmost column, all cell types are present in equal parts in the ground truth data. Cell types are then sequentially subtracted from the synthesized ground truth, starting with HSCs, until only NK cells remain. Error bars, s.d. from 100 random permutations. (**e**) Enhancer cytometry of ATAC-seq data derived from FACS-purified bone marrow CD34+ HSPCs. (**f**) Correlation of the fractional contribution for each HSPC cell type predicted by enhancer cytometry versus flow cytometry ground truth data for input CD34+ cells. The *x* axis presents the same data as in **e**.

identity, we compared GATA transcription factor footprints[27] between megakaryocyte–erythroid progenitor cells (MEPs) (GATA high) and common lymphoid progenitors (CLPs) (GATA low) and found that CLPs had no detectable binding at GATA sites when compared to MEPs (**Fig. 4d**).

We next reasoned that the accessibility of a given transcription factor motif should correlate with the expression of the associated transcription factor throughout hematopoiesis. However, the underlying motif sequence did not identify the precise causative regulator of accessibility at those motif instances. This is a common issue in epigenomic studies and is particularly important for cases in which many factors share identical or near-identical transcription factor motifs. To assign motifs to transcription factors, we integrated our ATAC-seq and RNA-seq data to predict causative regulators of motif accessibility (Online Methods, **Supplementary Fig. 9b–e**, and **Supplementary Table 4**). Using this approach, we found a striking correlation of motif

usage with the expression of known master regulators of hematopoiesis (**Fig. 4e**). For example, the expression of GATA1 and PAX5 was highly correlated with accessibility at GATA and PAX motifs, respectively ($r = 0.75$, $P = 1 \times 10^{-18}$ and $r = 0.88$, $P = 1 \times 10^{-230}$; **Fig. 4e–g** and **Supplementary Fig. 9f**). Interestingly, for some motifs, such as HOX, we found many putative regulators with weak correlations ($n = 11$; **Supplementary Fig. 9g,h**), suggesting that regulation of HOX accessibility is more complex. We provide the complete list of non-redundant transcription factor deviations, transcription factor motif–gene association table, and gene correlation analysis as an associated resource (**Supplementary Tables 3** and **4**, and **Supplementary Data**).

Regulome profiles chart the ontogeny of human diseases
In addition to enhancing understanding of developmental gene regulation, the hematopoietic regulome can trace the ontogeny of activity in the noncoding genome that influences human disease. Many genome-wide
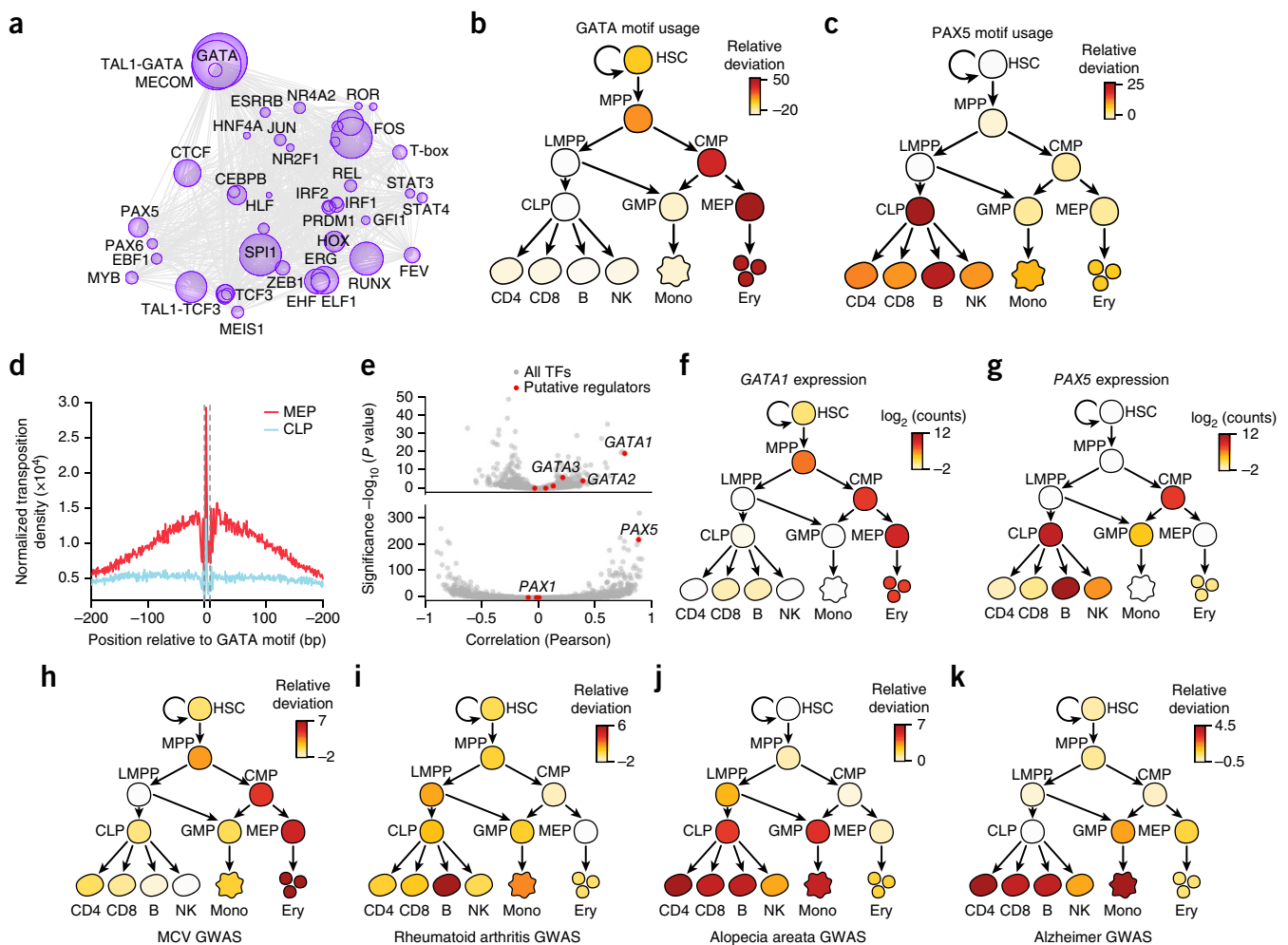
Figure 4 Integrative analysis of the hematopoietic regulome refines the transcriptional circuitry driving cell specification and enriches understanding of human disease. (**a**) Transcription factor dynamics showing major transcription factors driving hematopoietic regulomes. The size of each circle represents the effect of the corresponding motif in driving accessibility in human blood cells. The relative distance between circles represents the co-occurrence of motifs throughout hematopoietic differentiation (Online Methods). (**b,c**) Usage of GATA (**b**) and PAX5 (**c**) motifs throughout hematopoietic differentiation. Values represent the relative deviation of motif accessibility, a measure of motif usage in comparison to that in HSCs. (**d**) Footprint analysis of the GATA motif in MEP and CLP cells. (**e**) Pearson correlation of motif accessibility with transcription factor (TF) expression plotted against the significance of this correlation for GATA (top) and PAX (bottom) motifs. Red dots correspond to DNA-binding factors found in the analysis in **Supplementary Figure 9b** to bind the given motif. Gray dots represent all other DNA-binding factors. (**f,g**) Expression of *GATA1* (**f**) and *PAX5* (**g**) phenocopies usage of GATA (**b**) and PAX5 (**c**) motifs throughout hematopoietic differentiation. (**h–k**) Relative deviation scores of chromatin accessibility within hematopoietic regulatory elements with GWAS SNPs for MCV (**h**), rheumatoid arthritis (**i**), alopecia areata (**j**), and Alzheimer disease (**k**) (Online Methods). Darker red color is representative of enrichment of GWAS SNPs in open chromatin regions of the given cell type.

association studies (GWAS) have linked diseases to polymorphisms but have not been able to pinpoint the cells responsible for these phenotypes. By measuring the activity of regulatory elements that overlap regions with predicted sites of functional variation from GWAS, it now seems possible to more accurately predict the specific cell types affected by genetic variants linked to diverse human diseases (Online Methods, **Supplementary Fig. 10a–c**, and **Supplementary Note**)[28–30]. As an example, polymorphisms linked to mean corpuscular volume (MCV), a measure of the average volume of an

erythrocyte, were most strongly enriched in erythroblasts (**Fig. 4h**). Intriguingly, many regions associated with MCV polymorphisms first became accessible at the common myeloid progenitor (CMP) and MEP stages, suggesting that these polymorphisms may exert their effects before full erythroid lineage commitment. Similarly, we were able to predict involvement of various immune cell types in rheumatoid arthritis and less well-understood diseases such as alopecia areata and Alzheimer disease (**Fig. 4i–k**; see the **Supplementary Note** for further discussion).
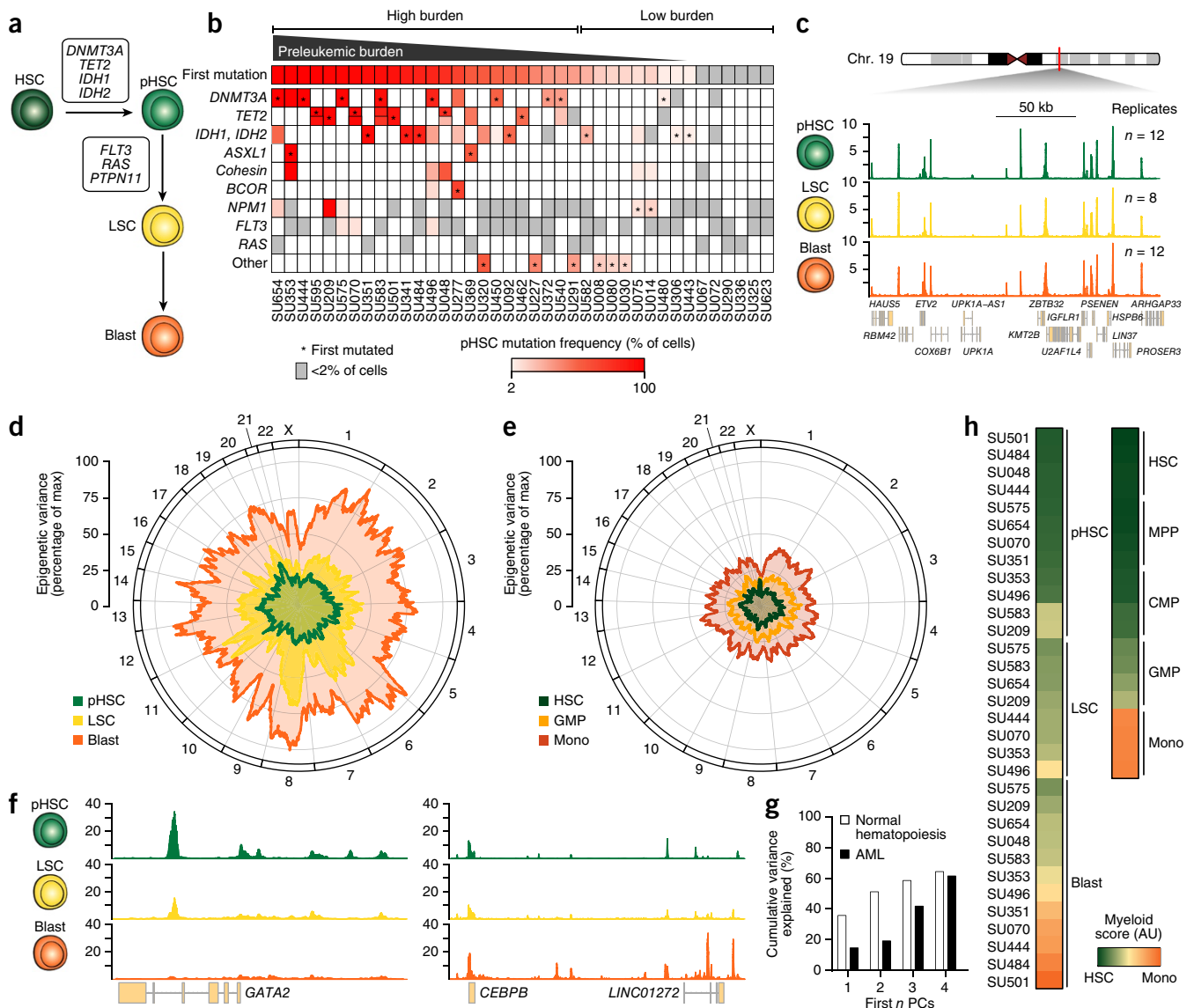
Figure 5 Acute myeloid leukemia regulomes show cooption of normal myelopoiesis. (**a**) Schematic of the leukemogenic process showing the genes mutated during each stage. (**b**) Mutation frequencies for HSCs isolated from patients with AML (n = 39). Color indicates the percentage of cells harboring mutation in a given gene, as estimated from variant allele frequency; gray indicates that a gene is mutated in leukemic cells but not in pHSCs (representing a late mutation event; detection threshold = 2% of cells, or 1% of alleles). An asterisk indicates the gene in which mutation is predicted to have occurred first. If a gene is mutated biallelically, the representative bar is divided in half. (**c**) Normalized ATAC-seq profiles at a control locus (chr. 19: 36,102,236–36,277,236) from FACS-purified AML cell types. Profiles represent the union of all biological replicates for each cell type. The y-axis scales range from 0–10 in normalized arbitrary units. (**d,e**) Mean variance in ATAC-seq signal across the linear genome, as calculated by a moving average for each leukemic cell stage (**d**) and its corresponding normal cell type (**e**) (Online Methods). Distance from the center of the plot represents variance; position along the circumference represents genomic position. (**f**) Normalized ATAC-seq profiles near *GATA2* (left; chr. 3: 128,197,777–128,218,433) and *CEBPB* (right; chr. 20: 48,800,260–48,904,715). The profiles shown are for SU444. The y-axis scales range from 0–10 in normalized arbitrary units. (**g**) Cumulative variance in AML ATAC-seq data explained by the first n principal components derived from normal hematopoiesis. (**h**) Myeloid development score derived from ATAC-seq data in normal blood cell types (n = 4 biological replicates) and AML cell types. AU, arbitrary units.

Leukemogenesis and cancer evolution in AML

To characterize the evolution of AML[31] in the context of normal hematopoiesis, we identified three distinct stages of AML evolution—preleukemic HSCs (pHSCs), leukemia stem cells (LSCs), and leukemic blast cells (blasts)—that can be enriched by FACS (**Supplementary Fig. 11a,b**). Current data indicate that HSCs serve as the reservoir for mutation acquisition during the early phases of leukemogenesis (**Fig. 5a**). Acquisition of founder mutations creates pHSCs that expand to create a preleukemic clone. Subsequent acquisition of progressor mutations generates LSCs that are capable of self-renewal and the production of AML blasts[32] (**Fig. 5a**).

Notably, the population of HSCs isolated from patients with leukemia by FACS represents a heterogeneous mixture of healthy, non-mutated HSCs and pHSCs. To quantify this heterogeneity, we define 'preleukemic burden' as the percentage of HSCs isolated from a patient with leukemia that harbor at least the first mutation. We profiled the frequency of known leukemogenic driver mutations in HSCs, T cells, and blasts from 39 patients with AML (**Supplementary Fig. 11c** and **Supplementary Table 5**). Preleukemic burden was highly variable in this cohort, with some patients exhibiting a complete repopulation of the HSC compartment with preleukemic cells and others exhibiting undetectable levels of preleukemic mutations (**Fig. 5b** and **Supplementary Fig. 11d**).

AML represents a cooption of normal myelopoiesis

The AML leukemogenic process provides a new system to study the genesis and evolution of cancer. The Fast-ATAC protocol produced robust accessibility profiles from cryopreserved patient-derived primary AML cells (**Fig. 5c**). We found that the level of variance in DNA accessibility across all samples of the same cell type increased
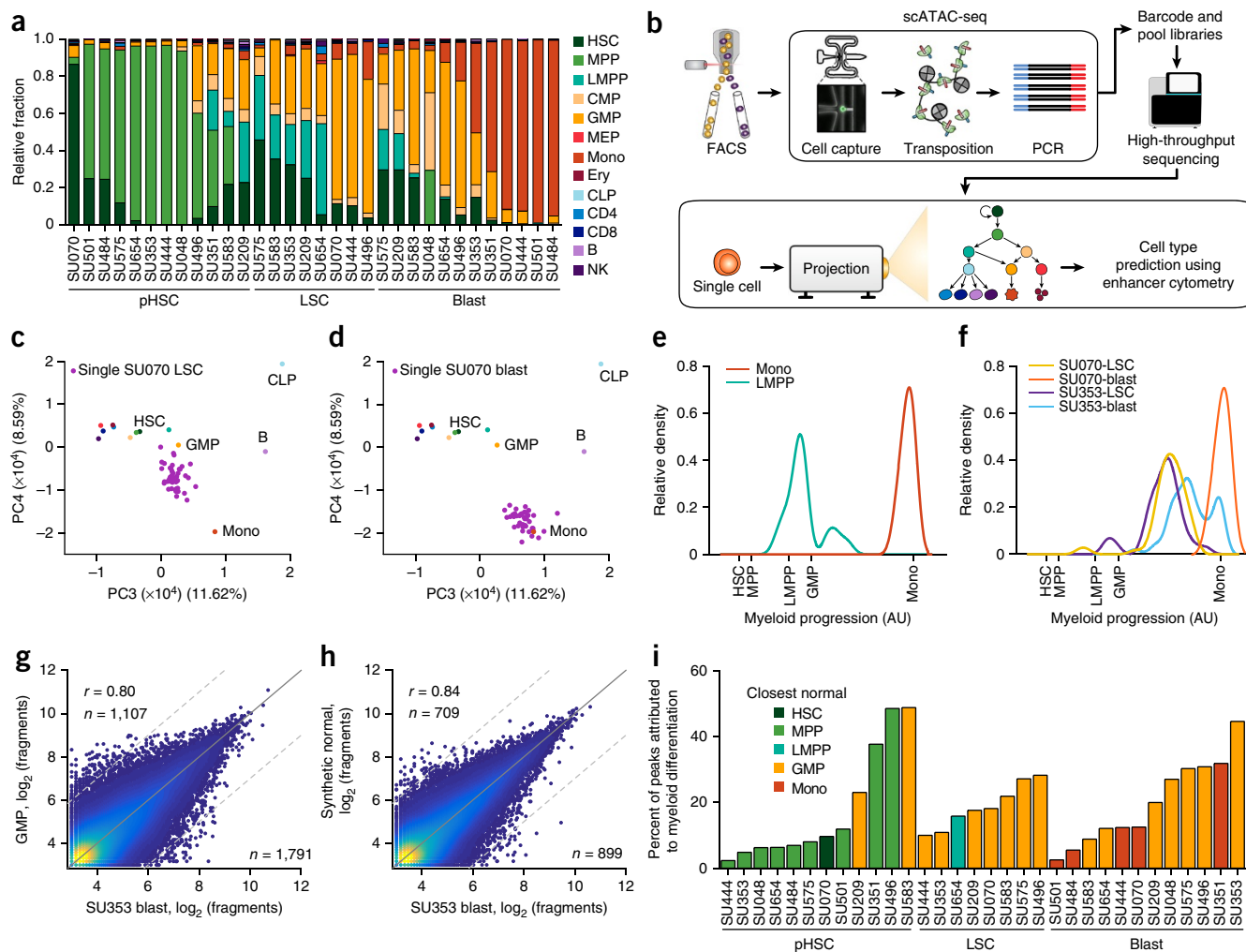

Figure 6 Enhancer cytometry and single-cell regulomes support a model of regulatory heterogeneity and allow for deconvolution of AML-specific biology. (**a**) Enhancer cytometry deconvolution showing the predicted contribution of various normal cell types to the regulatory landscape of different AML cell types. (**b**) Schematic of the scATAC-seq protocol and analysis (Online Methods). (**c,d**) Projection of ATAC-seq data derived from single SU070 LSCs ($n = 71$) (**c**) and single SU070 blasts ($n = 42$) (**d**) onto principal components derived from the normal hematopoietic hierarchy. (**e,f**) Relative densities of single LMPPs ($n = 68$) and monocytes ($n = 90$) (**e**) and of single SU070 LSCs ($n = 62$), SU070 blasts ($n = 42$), SU353 LSCs ($n = 36$), and SU353 blasts ($n = 52$) (**f**) projected onto a one-dimensional representation of myeloid developmental progression. AU, arbitrary units. (**g,h**) Scatterplots showing the correlation of ATAC-seq data derived from SU353 blasts with the closest normal cell type (GMP) (**g**) and enhancer cytometry–defined synthetic normal (**h**). The cutoff for differential peaks was a $\log_2$ (fold change) greater than 3. The r values reported were calculated from correlation of all peaks. Plots show 50,000 random peaks, each with at least five reads. (**i**) Comparison of AML cell types to synthetic normal analogs. For each sample, the closest normal cell type is indicated by the color of the bar. The percentage of the total significant peaks (called by comparison to the closest normal) that were removed by comparison to synthetic normal analogs is plotted for each sample.

through progressive stages of leukemia evolution (**Fig. 5d** and Online Methods). All AML cell types exhibited more between-donor sample-to-sample variance than the corresponding normal hematopoietic cells (**Fig. 5e**). This may be a manifestation of the point along the normal hematopoietic hierarchy at which the particular AML cell types exist. Indeed, key developmentally associated genes such as *GATA2* and *CEBPB* showed variation among the AML cell types consistent with different developmental stages (**Fig. 5f**), and we found that the first four principal components derived from normal hematopoietic differentiation accounted for much of the variation observed in our leukemia samples (**Fig. 5g** and Online Methods). Assigning a score to the myeloid differentiation component of our ATAC-seq data, we found that the various stages of AML spread across the trajectory from HSC to monocyte, indicating that the process of

leukemogenesis largely mirrors the process of normal myelopoiesis (**Fig. 5h** and **Supplementary Fig. 11e,f**). Consistent with their functional ability to produce both lymphoid and myeloid cells in xenotransplantation assays[11–13], pHSCs were most closely related to HSCs and MPPs (**Fig. 5h**). As shown previously[33], LSCs exhibited strong similarity to granulocyte–macrophage progenitor cells (GMPs) and lymphoid–primed multipotent progenitor cells (LMPPs) and leukemic blasts showed a wider distribution, with less differentiated blasts clustering with GMP cells and more differentiated blasts clustering with monocytes[34,35] (**Fig. 5h**).

AML cell types exhibit regulatory heterogeneity

The observed developmental positions across myelopoiesis suggest that each patient-specific AML might harbor a unique collection
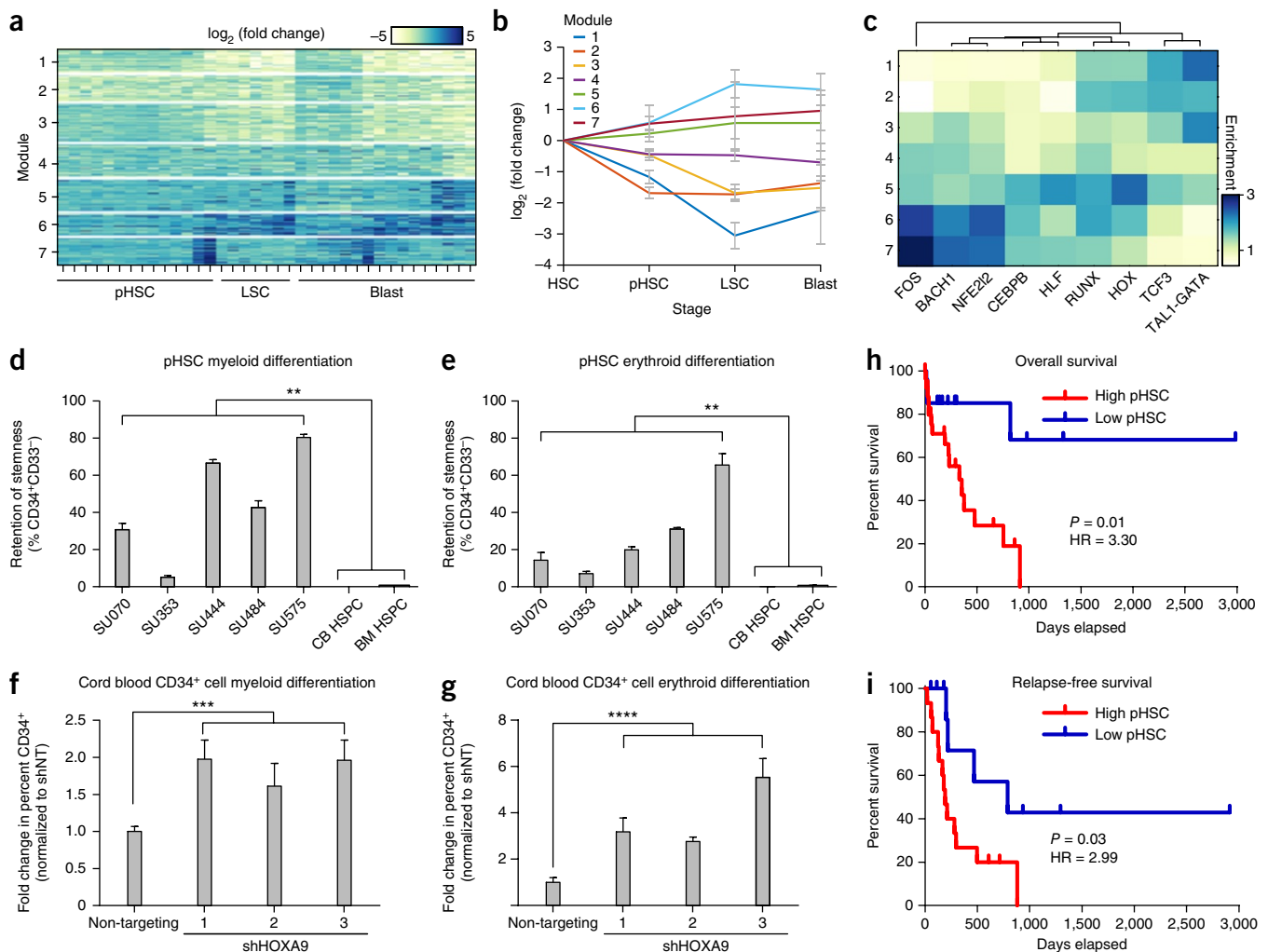

Figure 7 Early chromatin accessibility alterations in pHSCs cause defects in differentiation that correlate with adverse patient outcomes. (**a**) *k*-means clustering was used to identify seven clusters of covarying peaks, termed regulatory modules (Online Methods). (**b**) Enrichment of each regulatory module from **a** at each stage of leukemia evolution. All biological replicates for each AML cell type were merged. Error bars, 1 s.d. across all samples of that given cell type. (**c**) Enrichment and hierarchical clustering of transcription factor motifs enriched in each of the seven AML-specific regulatory modules. (**d,e**) Retention of CD34 expression, as measured by flow cytometry analysis, after 6 d of enforced differentiation down the myeloid (**d**) or erythroid (**e**) lineage. Error bars, 1 s.d. Experiments were performed in triplicate. (**f,g**) Fold change in the percentage of cells expressing CD34 as measured by flow cytometry analysis of cord blood–derived HSCs transduced with shRNAs targeting *HOXA9* (shHOXA9) or a non-targeting control. CD34 expression was measured after 6 d of differentiation down the myeloid (**f**) or erythroid (**g**) lineage. Only GFP-positive transduced cells were analyzed. Error bars, 1 s.d. Experiments were carried out in triplicate. *P* values in **d**–**g** were derived from two-tailed *t* tests: ***P < 0.01, ****P < 0.001, *****P < 0.0001. (**h,i**) Overall (**h**) and relapse-free (**i**) survival of patients stratified by preleukemic burden (high burden, *n* = 24; low burden, *n* = 15). High preleukemic burden was defined by >20% of HSCs harboring at least the first preleukemic mutation. *P* values comparing the two Kaplan–Meier survival curves were calculated using the log-rank (Mantel–Cox) test. Hazard ratios (HRs) were determined using the Mantel–Haenszel approach.

of multiple distinct normal regulatory programs. Using enhancer cytometry, we quantified the contribution of each normal cell type to each leukemic sample assayed (**Fig. 6a**, **Supplementary Fig. 12a**, and **Supplementary Table 6**). We found that each patient, at each stage of leukemogenesis, harbored regulatory contributions from multiple distinct normal cell types that are often developmentally distinct from each other. This result raises the intriguing possibility that individual AML cells might either (i) exist in mixed cell states that are not typically maintained during normal hematopoiesis or (ii) show cellular heterogeneity, wherein a mixture of cell states exists within the leukemic clone. Notably, we found that the majority of the patient donors had AML blasts that were clonally derived and harbored all the leukemic mutations at comparable allele frequencies (**Supplementary Table 5**), suggesting that the epigenomic diversity observed through enhancer cytometry is not related to genetic heterogeneity of AML cells.

To discriminate between these two possibilities, we performed single-cell ATAC-seq (scATAC-seq) on purified LSCs and blasts from two patients with AML and compared these samples to myeloid cells from healthy donors. We then performed enhancer cytometry using principal-component analysis (PCA) trained on our ensemble ATAC-seq data (**Fig. 6b** and Online Methods). This analytical framework was validated by projection of downsampled bulk ATAC-seq data (**Supplementary Fig. 12b,c**) and enabled accurate projection of single-cell accessibility profiles onto hematopoietic principal components (**Fig. 6c,d** and **Supplementary Fig. 12d,e**). The relationship between developmental progression and single-cell chromatin accessibility could be further visualized as a one-dimensional histogram (**Fig. 6e,f**, Online Methods, and **Supplementary Fig. 12f**).

For normal physiological comparison, we performed scATAC-seq on normal monocytes ($n = 88$) and LMPPs ($n = 94$) isolated from healthy donors. Single LMPP and monocyte cells showed myelopoietic developmental projection scores centered at the predicted ensemble scores (**Fig. 6e**). In contrast, AML cells were either uniformly centered at developmentally intermediate states (for example, SU070 LSCs with unimodal peaks located between normal LMPPs and monocytes in **Fig. 6f**) or alternatively showed broad bimodal distributions representing regulomes from both intermediate and developmentally normal cell states (for example, SU353 LSCs and blasts; **Fig. 6f**). In addition, widely used cell lines, such as the AML line HL60, also showed a unimodal and mixed normal cell regulome, observed by ensemble and single-cell ATAC-seq (**Supplementary Fig. 12g–i**). These results show that the regulatory heterogeneity observed in the ensemble profiles of AML samples can arise from both single-cell intra- and intercellular heterogeneity (see the **Supplementary Note** for an extended discussion).

Synthetic normal analogs uncover AML-specific biology

The ability to accurately quantify the contribution of each normal cell regulome to the epigenetic profile of a leukemic cell type enables more robust identification of AML-specific regulatory elements. In particular, analyses of leukemic cell types in the past have relied on comparing malignant cells to a carefully chosen normal cell type (for example, GMPs). Here, because of the regulatory heterogeneity in AML, we reasoned that an effective normal cell comparison would be possible with the generation of 'synthetic normals' that represent admixtures of various normal cells defined by enhancer cytometry (Online Methods). Although comparison of AML cell types to their closest normal cell analogs yielded a high correlation ($r = 0.80$; **Fig. 6g**), comparison of AML cell types to their synthetic normal analogs yielded higher correlation ($r = 0.84$; **Fig. 6h** and **Supplementary**

Fig. 13a) and, more notably, led to a reduction in the number of AML-specific peaks identified ($n = 899$ compared to $n = 1,791$; **Fig. 6i** and **Supplementary Fig. 13b,c**). Moreover, comparing samples to the synthetic normal from each individual AML cell type reduced global measures of epigenetic variance (**Supplementary Fig. 13d** compared to **Fig. 5d**).

To identify clusters of coordinately regulated elements, fold change values between each AML and its synthetic normal were clustered using k-means clustering to identify seven distinct regulatory modules (**Fig. 7a**, Online Methods, and **Supplementary Fig. 14a**). Usage of these modules was tracked through leukemogenesis to identify patterns related to specific AML cell types (**Fig. 7b**). Each module showed enrichment for peaks associated with different key transcription factors (**Fig. 7c**). For example, modules 6 and 7 showed strong enrichment for JUN and FOS activity. Similar observations of increased JUN/FOS accessibility have been made from DNase-seq data in *FLT3-ITD*–positive AML[20], suggesting that this result may be related to the high prevalence of *FLT3* mutations in our patient cohort. This increase in accessibility of JUN/FOS motifs was reflected by an increase in expression of these factors by RNA-seq (**Supplementary Fig. 14b**) and was maintained through the stages of leukemogenesis, identifying inhibition of these pathways as a potential therapeutic strategy in AML (**Supplementary Fig. 14c–e**). This observation is consistent with previous publications that identified overexpression of *JUN* in AML[36] and found c-JUN N-terminal kinase (JNK) inhibition to be a putative therapeutic strategy[37,38] and indicate that similar strategies may prove efficacious in targeting pHSCs.

Mechanism and consequences of pHSC clonal advantage

Using ATAC-seq and enhancer cytometry, we show that pHSCs share many regulatory programs with HSCs and MPPs (**Fig. 6a**). Nevertheless, comparison to synthetic normal analogs identified distinct regulatory modules (modules 1 and 2) that showed decreased accessibility in pHSCs, representing the earliest known event of AML evolution (**Fig. 7b**). These repressed regulatory modules are enriched for motifs associated with HSPCs (HOX, RUNX, and GATA) and provide direct evidence to support a model in which pHSCs maintain a unique epigenetic and functional state.

To better understand the consequences of loss in accessibility at motifs associated with HSPCs, we probed pHSCs for phenotypic changes related to self-renewal and differentiation. When pHSCs were induced to differentiate down the myeloid and erythroid lineages (**Supplementary Fig. 14f**), pHSCs showed strong resistance to differentiation, instead favoring maintenance of the stem cell immunophenotype as indicated by retention of CD34 expression (**Fig. 7d,e**). We hypothesized that the observed decreased accessibility at HOX transcription factor motifs might mediate the observed retention of stem cell immunophenotype. Indeed, depletion of one such HOX factor, *HOXA9*, by short hairpin RNA (shRNA)-mediated knockdown (**Supplementary Fig. 14g** and **Supplementary Table 7**) in umbilical cord blood CD34+ HSPCs led to retention of stem cell immunophenotype in the context of both myeloid (**Fig. 7f**) and erythroid (**Fig. 7g**) differentiation. Moreover, a concomitant decrease in differentiated granulocytes and erythroid cells was also observed (**Supplementary Fig. 14h–j**), consistent with results from mouse models of HOXA9 deficiency[39,40]. Together, these results suggest that decreased HOX accessibility in pHSCs may promote retention of stem cell characteristics and prevent differentiation of these cells. Additional HOX factors may have a role in defective pHSC differentiation, as the role of HOXA9 in hematopoiesis and leukemogenesis is complex[39–41].

pHSC resistance to differentiation potentially explains the observation that pHSCs outcompete their normal HSC counterparts *in vivo* (**Fig. 5b** and **Supplementary Fig. 14k**). pHSCs would gain an evolutionary advantage while promoting an HSC-like state and thus increase the likelihood of acquiring additional leukemogenic mutations. One implication of this model is that preleukemic burden may have adverse effects on patient survival, despite the fact that pHSCs do not confer disease in xenograft transplant assays[11–13]. Characterization of our patient cohort showed that preleukemic burden inversely correlated with overall and relapse-free survival (hazard ratio = 3.30 for overall survival and 2.99 for relapse-free survival, $P < 0.05$; **Fig. 7h,i**). These results further implicate pHSCs in AML pathology and suggest a mechanism whereby AML arises from a preleukemic clone that is capable of outcompeting its normal HSC counterparts (**Supplementary Fig. 14k**), which predisposes patients to more aggressive or therapy-refractory leukemia.

DISCUSSION

Here we report a rich resource charting the epigenomic and transcriptomic landscape of 16 unique blood cell types. This resource relies on accurate and precise determination of the regulome landscapes in primary human blood cells, made possible by Fast-ATAC. Unsupervised clustering of accessible chromatin regions, specifically distal elements, groups individual cell types with high cluster purity (91% for ATAC-seq in comparison to 78% for RNA-seq), suggesting that these distal regulatory elements more precisely define cell identity and developmental trajectory. Enhancer cytometry harnesses this specificity and enumerates the frequencies of pure cell types in complex cell mixtures. This technique may be applicable to address cell type heterogeneity in other contexts of stem cell biology or cell therapy.

Additionally, this atlas of human hematopoiesis enriches the interpretation of GWAS results in several ways. We identify strong associations of disease-linked polymorphisms with the open chromatin landscapes of specific hematopoietic cell types, potentially uncovering the developmental contexts in which the disease-relevant elements first become active. In the case of MCV, the strongest association occurs in erythroblast cells, but a significant association can be seen as early as the CMP stage. These results are consistent with the concept that many enhancers are developmentally primed before their activation following cell differentiation[3]. Our resource further provides a platform to identify specific *trans* regulators that drive blood cell identity and function. Integration of ATAC-seq and RNA-seq data improves motif–transcription factor pairing and can facilitate the determination of causative regulators of chromatin accessibility throughout hematopoietic differentiation. We anticipate that this combined data set, which represents a dynamic developmental process, will be a rich resource for continued efforts to build computational tools that model both *cis*[42] and *trans*[43] determinants of chromatin accessibility and gene expression.

Application of this resource to the study of three distinct time points in AML evolution sheds light on the biology and stepwise progression of leukemia evolution. A longstanding debate in cancer biology is how cancer cells violate cell lineage rules[44,45], for example, by maintaining self-renewal in an otherwise differentiated cell state. By using our comprehensive map of hematopoiesis, patient-matched AML cell subsets, and scATAC-seq data for hundreds of individual leukemic and normal cells, we show evidence of regulatory heterogeneity in the epigenome—a single cell with several normally distinct regulatory programs (**Supplementary Note**). We find that such mixed regulatory programs may be the result of both intra- and intercellular regulatory heterogeneity.

This regulatory heterogeneity suggests that there might be no appropriate 'normal' for tumor–normal comparisons in epigenomic and transcriptomic studies. Instead, we use enhancer cytometry to construct synthetic normals—proportionally matching the predicted fractional contribution of cell-type-specific regulomes from normal hematopoiesis—to pinpoint cancer-specific aberrations. This approach led us to identify loss of HOX-mediated accessibility as the most consistent defect in pHSCs. We found that loss of a HOX factor can, in fact, cause defects in differentiation similar to those observed in pHSCs and potentially confer an evolutionary advantage. Notably, higher preleukemic burden is predictive of poor overall and relapse-free survival in AML, indicating an important role for pHSCs in pathogenesis.

The methodologies developed here for the study of AML have important implications for the study of other blood and solid tumor malignancies. We anticipate that regulatory heterogeneity is a widespread phenomenon in many types of cancer and that our integrative approach using enhancer cytometry to construct synthetic normal analogs could be broadly applicable to many pathologies. Future studies harnessing the power of enhancer cytometry to understand other cancer-specific regulatory networks could provide key insights into the aberrations that drive the formation and persistence of malignant disease. Thus, we believe that this work provides a methodological framework for the paradigm of mapping regulomes of normal tissues to better understand the ontogeny of human disease.

URLs. JASPAR, http://jaspar.genereg.net/; UCSC Genome Browser Track Hub, https://s3-us-west-1.amazonaws.com/chang-public-data/2016_NatGen_ATAC-AML/hub.txt.

METHODS

Methods and any associated references are available in the online version of the paper.

Note: Any Supplementary Information and Source Data files are available in the online version of the paper.

AUTHOR CONTRIBUTIONS

M.R.C., J.D.B., R.M., and H.Y.C. conceived the project. M.R.C. performed all cell sorting, RNA-seq, and CIBERSORT analysis, AML cell culture experiments, and

1. Quesenberry, P.J. & Colvin, G.A. in *Williams Hematology* 153–174 (McGraw-Hill, 2005).
2. Ji, H. *et al.* Comprehensive methylome map of lineage commitment from haematopoietic progenitors. *Nature* **467**, 338–342 (2010).
3. Lara-Astiaso, D. *et al.* Chromatin state dynamics during blood formation. *Science* **345**, 943–949 (2014).
4. Chen, L. *et al.* Transcriptional diversity during lineage commitment of human blood progenitors. *Science* **345**, 1251033 (2014).
5. Novershtern, N. *et al.* Densely interconnected transcriptional circuits control cell states in human hematopoiesis. *Cell* **144**, 296–309 (2011).
6. Buenrostro, J.D., Giresi, P.G., Zaba, L.C., Chang, H.Y. & Greenleaf, W.J. Transposition of native chromatin for fast and sensitive epigenomic profiling of open chromatin, DNA-binding proteins and nucleosome position. *Nat. Methods* **10**, 1213–1218 (2013).
7. Jin, W. *et al.* Genome-wide detection of DNase I hypersensitive sites in single cells and FFPE tissue samples. *Nature* **528**, 142–146 (2015).
8. Shih, A.H. *et al.* The role of mutations in epigenetic regulators in myeloid malignancies. *Nat. Rev. Cancer* **12**, 599–612 (2012).
9. Genovese, G. *et al.* Clonal hematopoiesis and blood-cancer risk inferred from blood DNA sequence. *N. Engl. J. Med.* **371**, 2477–2487 (2014).
10. Jaiswal, S. *et al.* Age-related clonal hematopoiesis associated with adverse outcomes. *N. Engl. J. Med.* **371**, 2488–2498 (2014).
11. Jan, M. *et al.* Clonal evolution of preleukemic hematopoietic stem cells precedes human acute myeloid leukemia. *Sci. Transl. Med.* **4**, 149ra118 (2012).
12. Corces-Zimmerman, M.R., Hong, W.-J., Weissman, I.L., Medeiros, B.C. & Majeti, R. Preleukemic mutations in human acute myeloid leukemia affect epigenetic regulators and persist in remission. *Proc. Natl. Acad. Sci. USA* **111**, 2548–2553 (2014).
13. Shlush, L.I. *et al.* Identification of pre-leukaemic haematopoietic stem cells in acute leukaemia. *Nature* **506**, 328–333 (2014).
14. Majeti, R., Park, C.Y. & Weissman, I.L. Identification of a hierarchy of multipotent hematopoietic progenitors in human cord blood. *Cell Stem Cell* **1**, 635–645 (2007).
15. Manz, M.G., Miyamoto, T., Akashi, K. & Weissman, I.L. Prospective isolation of human clonogenic common myeloid progenitors. *Proc. Natl. Acad. Sci. USA* **99**, 11872–11877 (2002).
16. Kohn, L.A. *et al.* Lymphoid priming in human bone marrow begins before expression of CD10 with upregulation of L-selectin. *Nat. Immunol.* **13**, 963–971 (2012).
17. Seita, J. & Weissman, I.L. Hematopoietic stem cell: self-renewal versus differentiation. *Wiley Interdiscip. Rev. Syst. Biol. Med.* **2**, 640–653 (2010).
18. Roadmap Epigenetics Consortium. *et al.* Integrative analysis of 111 reference human epigenomes. *Nature* **518**, 317–330 (2015).
19. Manning, C.D., Raghavan, P. & Schutze, H. *Introduction to Information Retrieval* (Cambridge University Press, 2008).
20. Cauchy, P. *et al.* Chronic FLT3–ITD signaling in acute myeloid leukemia is connected to a specific chromatin signature. *Cell Rep.* **12**, 821–836 (2015).
21. Heinz, S. *et al.* Simple combinations of lineage-determining transcription factors prime *cis*-regulatory elements required for macrophage and B cell identities. *Mol. Cell* **38**, 576–589 (2010).
22. Newman, A.M. *et al.* Robust enumeration of cell subsets from tissue expression profiles. *Nat. Methods* **12**, 453–457 (2015).
23. Buenrostro, J.D. *et al.* Single-cell chromatin accessibility reveals principles of regulatory variation. *Nature* **523**, 486–490 (2015).
24. Weiss, M.J. & Orkin, S.H. GATA transcription factors: key regulators of hematopoiesis. *Exp. Hematol.* **23**, 99–107 (1995).
25. Burns, C.E., Traver, D., Mayhall, E., Shepard, J.L. & Zon, L.I. Hematopoietic stem cell fate is established by the Notch–Runx pathway. *Genes Dev.* **19**, 2331–2342 (2005).
26. Nerlov, C. & Graf, T. PU.1 induces myeloid lineage commitment in multipotent hematopoietic progenitors. *Genes Dev.* **12**, 2403–2412 (1998).
27. Neph, S. *et al.* An expansive human regulatory lexicon encoded in transcription factor footprints. *Nature* **489**, 83–90 (2012).
28. Gjoneska, E. *et al.* Conserved epigenomic signals in mice and humans reveal immune basis of Alzheimer's disease. *Nature* **518**, 365–369 (2015).
29. Farh, K.K. *et al.* Genetic and epigenetic fine mapping of causal autoimmune disease variants. *Nature* **518**, 337–343 (2015).
30. Maurano, M.T. *et al.* Systematic localization of common disease-associated variation in regulatory DNA. *Science* **337**, 1190–1195 (2012).
31. Döhner, H., Weisdorf, D.J. & Bloomfield, C.D. Acute myeloid leukemia. *N. Engl. J. Med.* **373**, 1136–1152 (2015).
32. Bonnet, D. & Dick, J.E. Human acute myeloid leukemia is organized as a hierarchy that originates from a primitive hematopoietic cell. *Nat. Med.* **3**, 730–737 (1997).
33. Goardon, N. *et al.* Coexistence of LMPP-like and GMP-like leukemia stem cells in acute myeloid leukemia. *Cancer Cell* **19**, 138–152 (2011).
34. Bennett, J.M. *et al.* Proposals for the classification of the acute leukaemias. French-American-British (FAB) co-operative group. *Br. J. Haematol.* **33**, 451–458 (1976).
35. van't Veer, M.B. The diagnosis of acute leukemia with undifferentiated or minimally differentiated blasts. *Ann. Hematol.* **64**, 161–165 (1992).
36. Rangatia, J. *et al.* Elevated c-Jun expression in acute myeloid leukemias inhibits C/EBPα DNA binding via leucine zipper domain interaction. *Oncogene* **22**, 4760–4764 (2003).
37. Volk, A. *et al.* Co-inhibition of NF-κB and JNK is synergistic in TNF-expressing human AML. *J. Exp. Med.* **211**, 1093–1108 (2014).
38. Hartman, A.D. *et al.* Constitutive c-Jun N-terminal kinase activity in acute myeloid leukemia derives from Flt3 and affects survival and proliferation. *Exp. Hematol.* **34**, 1360–1376 (2006).
39. Magnusson, M., Brun, A.C.M., Lawrence, H.J. & Karlsson, S. *Hoxa9*/*Hoxb3*/*Hoxb4* compound null mice display severe hematopoietic defects. *Exp. Hematol.* **35**, 1421–1428 (2007).
40. Lawrence, H.J. *et al.* Mice bearing a targeted interruption of the homeobox gene *HOXA9* have defects in myeloid, erythroid, and lymphoid hematopoiesis. *Blood* **89**, 1922–1930 (1997).
41. Thorsteinsdottir, U. *et al.* Overexpression of the myeloid leukemia–associated *Hoxa9* gene in bone marrow cells induces stem cell expansion. *Blood* **99**, 121–129 (2002).
42. González, A.J., Setty, M. & Leslie, C.S. Early enhancer establishment and regulatory locus complexity shape transcriptional programs in hematopoietic differentiation. *Nat. Genet.* **47**, 1249–1259 (2015).
43. Whitaker, J.W., Chen, Z. & Wang, W. Predicting the human epigenome from DNA motifs. *Nat. Methods* **12**, 265–272 (2015).
44. Macedo, A. *et al.* Characterization of aberrant phenotypes in acute myeloblastic leukemia. *Ann. Hematol.* **70**, 189–194 (1995).
45. Tiacci, E. *et al.* PAX5 expression in acute leukemias: higher B-lineage specificity than CD79a and selective association with t(8;21)-acute myelogenous leukemia. *Cancer Res.* **64**, 7399–7404 (2004).

ONLINE METHODS

Availability of sequencing data. All sequencing data are available through the Gene Expression Omnibus (GEO) via accession GSE74912. Additionally, the data from normal hematopoietic cells have been made available as a UCSC Genome Browser Track Hub (see URLs) and as a Washington University EpiGenome Browser session (ID XVqu0IKMi1).

Human samples. Normal donor human bone marrow and peripheral blood cells were obtained fresh from AllCells or the Stanford Blood Center. All normal blood cell populations were sorted fresh. Human AML samples were obtained from patients at the Stanford Medical Center with informed consent, according to institutional review board (IRB)-approved protocols (Stanford IRB, 18329 and 6453). Mononuclear cells from each sample were isolated by Ficoll separation, resuspended in 90% FBS + 10% DMSO, and cryopreserved in liquid nitrogen. All analyses conducted here on AML cells used freshly thawed cells. The criteria for inclusion of AML samples were pre-established. Samples were selected solely on the basis of the availability of an adequate number of cells. For normal donors, no exclusion criteria were used.

Definition of cell types isolated. Here we isolated HSCs, LSCs, and blasts from patients with AML. These cells were defined by immunophenotype (**Supplementary Table 1**), as demonstrated previously[46]. The patients examined by ATAC-seq and RNA-seq in this study were selected in such a way that >80% of the HSCs were preleukemic.

Additionally, we isolated multiple different normal cell types from healthy donors (**Supplementary Table 1**). Mature granulocytes were excluded from our analyses because of high endogenous RNase and protease levels. Mature megakaryocytes proved difficult to isolate at adequate cell numbers and were similarly excluded.

Cell lines. Cell line data were downloaded from GEO accession GSE65360.

Flow cytometry analysis and cell sorting. All antibodies used for flow cytometry are detailed in **Supplementary Table 1**.

To prepare cells for FACS, all cells were recovered for 20 min at 37 °C in the presence of 200 U/ml DNase (Worthington Biochemical) in IMDM with 10% FBS. After recovery, viable mononuclear cells were separated by a Ficoll density gradient (GE Healthcare). When necessary, CD34-based enrichment was performed using paramagnetic MACS beads (Miltenyi Biotech) according to the manufacturer's protocol.

FACS sorting was performed on a Becton Dickinson FACSAria II. All cells were resuspended in and sorted into cold FACS buffer (PBS + 2% FBS + 2 mM EDTA) containing propidium iodide at 1 μg/ml or DAPI at 1 μg/ml. All cell sorting steps were validated using post-sort analyses to verify the purity of the sorted cell populations (**Supplementary Table 1**).

Transcriptome sequencing. RNA was isolated from 1,000–100,000 FACS-purified cells using the Qiagen RNeasy Plus Micro kit. RNA quality was verified on an Agilent Bioanalyzer Pico Eukaryote chip. Five microliters of total RNA (300 pg–80 ng) was used as input for the NuGen Ovation V2 cDNA synthesis kit. SPIA-amplified cDNA was sheared using a Covaris S2 sonicator as follows: 10% duty cycle, 5 intensity, 100 cycles/burst, 5 min, 120-μl volume. Sheared cDNA was purified and size selected using AMPure XP beads at a 0.9:1 beads-to-sample ratio. After cleanup, Illumina TruSeq adaptors were ligated onto the cDNA using the NEBNext Ultra library preparation kit according to the manufacturer's instructions. Library quality and concentration were determined using an Agilent Bioanalyzer HS DNA chip and a Qubit fluorometer. Libraries were sequenced to an average depth of 12 million read pairs per sample.

Transcriptome data analysis. RNA-seq data were aligned to the human reference genome (GRCh37/hg19) using STAR with standard input parameters. Aligned reads were filtered for reads that mapped uniquely to non-mitochondrial regions. Duplicate reads were removed using Picard MarkDuplicates. Transcript counts were produced using HTseq against the UCSC refGene transcriptome. Transcript counts were processed using DESeq2, normalizing for both library size and transcript GC content using conditional quantile normalization[47]. Differential expression was determined without the use of a Cooks cutoff. All downstream analyses on RNA-seq data were performed on variance-stabilizing transformed data obtained from DESeq2.

Fast-ATAC sequencing. This protocol has been optimized for blood cells. We note that digitonin is a gentle detergent and this protocol may not be ideal for cell lines and other cell types that are more resistant to lysis. Five thousand sorted cells in FACS buffer were pelleted by centrifugation at 500*g* RCF for 5 min at 4 °C in a precooled fixed-angle centrifuge. All supernatant was removed using two pipetting steps, being careful to not disturb the cell pellet, which was not visible. Fifty microliters of transposase mixture (25 μl of 2× TD buffer, 2.5 μl of TDE1, 0.5 μl of 1% digitonin, and 22 μl of nuclease-free water) (FC-121-1030, Illumina; G9441, Promega) was added to the cells, and the pellet was disrupted by pipetting. Transposition reactions were incubated at 37 °C for 30 min in an Eppendorf ThermoMixer with agitation at 300 rpm. Transposed DNA was purified using a QIAGEN MinElute Reaction Cleanup kit (28204), and purified DNA was eluted in 10 μl of elution buffer (10 mM Tris-HCl, pH 8). Transposed fragments were amplified and purified as described previously[48] with modified primers[23]. Libraries were quantified using qPCR before sequencing. All Fast-ATAC libraries were sequenced using paired-end, dual-index sequencing on a NextSeq instrument with 76 × 8 × 8 × 76 cycle reads.

ATAC-seq data analysis. ATAC-seq data were processed as previously described[23] with notable exceptions. In brief, reads were trimmed using a custom script and aligned using Bowtie 2. To call peaks, data were aggregated by each unique cell type, and peak summits were called using MACS2 and filtered using a custom blacklist, as previously described[23].

To generate a non-redundant list of hematopoiesis- and cancer-related peaks, we first extended summits to 500-bp windows (±250 bp). We then ranked the 500-bp peaks by summit significance value (defined by MACS2) and chose a list of non-overlapping, maximally significant peaks. The complete data set comprised a total of 590,650 peaks. To annotate peaks with promoter and distal labels and the nearest gene, we used the HOMER package with command annotatePeaks.pl. As described previously[23], we counted fragments for each sample across all 590,650 peaks to provide a count matrix. To obtain normalized fragment counts, which were used for all downstream processing, we first performed quantile normalization followed by GC content normalization (CQN R package[47]). Data tracks, used solely for visualization, were normalized to the number of fragments falling within all peaks for each sample. Coverage tracks were visualized using the Gviz R package. Fragment yield (**Supplementary Fig. 1e**) was computed by multiplying the library diversity calculated using Picard tools by the number of reads falling within peaks; values were then divided by the number of cells used in each assay.

For information on transcription factor–based analyses, see the **Supplementary Note**.

Unsupervised hierarchical clustering. Unless otherwise stated, all hierarchical clustering was unsupervised, using Pearson correlation as the distance metric, and was performed on all relevant features (for ex. all genes for RNA-seq or all peaks for ATAC-seq). All clustering analyses were performed on normalized data.

Cluster purity. Cluster purity was calculated as described previously[19]. Briefly, 13 clusters were defined as branches of the dendrogram, representing all individual replicates without overlap. Each cluster was assigned to the cell type that was most frequent in the cluster. In this way, there was one cluster (branch) that was assigned to represent each cell type. For each cluster, the accuracy of this assignment was measured by counting the number of correctly assigned experiments. For example, if the HSC cluster contained three HSC experiments and two MPP experiments, this cluster would be given a value of three. The sum of the number of correctly assigned experiments was divided by the total number of experiments to obtain cluster purity.

GWAS analysis. Using a list of blood-enriched GWAS, we applied the deviation pipeline (as described in the **Supplementary Note** for transcription

factor motifs), using an identical approach in which each GWAS disease was analogous to a transcription factor motif and each GWAS peak association was analogous to an individual transcription factor motif occurrence in a peak. For more information, see the **Supplementary Note**.

CIBERSORT application, benchmarking, and signature matrix generation. CIBERSORT v1.0.1 was used as recommended by the authors. Test set data and training set data represented unique non-overlapping samples. Benchmarking was performed using randomly permuted synthetic data. For each test, a unique signature matrix was generated from $n - 1$ replicates of each cell type (leave one out). This signature matrix was used to deconvolve ten randomly permuted cellular mixtures derived from the replicate that was excluded from the training set and signature matrix. One hundred unique permutations were performed, ten permutations each on ten different training sets.

The curated CIBERSORT signature matrix (**Supplementary Table 2**) was generated using default CIBERSORT parameters. To define a list of distal elements for input into CIBERSORT, we filtered peaks by removing peaks mapping to sex chromosomes, promoter and TSS regions (±1 kb), and regions found to be highly accessible in AML samples when compared to the closest normal cell type. Artifactual peaks were also removed using a custom blacklist. These regions were removed to prevent bias based on donor sex, to enhance cell-type-specific patterns, and to avoid overfitting of AML samples to normal cell types respectively.

Generation of synthetic normal analogs. Synthetic normal analogs were generated on the basis of fractional contributions predicted by CIBERSORT (**Supplementary Table 6**). For each AML sample, a synthetic normal analog was generated by multiplying the fractional contribution of each normal cell type by the normalized fragment number for that cell type. This was done on a peak-by-peak basis, and values were summed for each peak to give the synthetic normal value. For example, assuming a given sample has fractional contributions of 0.3 for HSCs, 0.5 for MPPs, 0.2 for CMPs, and 0 for all other cell types, a synthetic normal analog for peak 1 would be constructed by taking the sum of the average HSC normalized fragments multiplied by 0.3, the MPP normalized fragments multiplied by 0.5, the CMP normalized fragments multiplied by 0.2, and zero for all other cell types. Synthetic normal analogs were then quantile normalized with the leukemic sample of interest.

Cancer modules. To calculate differences for tumor–synthetic normal pairs, we computed $\log_2$ (fold change) values from the AML sample of interest to the corresponding synthetic normal. Notably, samples SU209-pHSC and SU583-pHSC were removed from this analysis. These samples appeared to be outliers in that they were more developmentally mature and exhibited an unexpectedly large number of differential peaks (**Supplementary Fig. 13b**). To determine unique cancer-specific regulatory modules, we first filtered for significantly altered peaks using a cutoff of $\log_2$ (fold change) greater than 4 or less than −4, resulting in 6,752 peaks. To determine AML-specific regulatory modules, we used k-means analysis to cluster the significantly altered peaks. $k = 7$ was selected by analyzing the mean centroid distances for each cluster (Euclidean) for k values increasing from 1 to 20 (**Supplementary Fig. 14a**) where $k = 7$ approximated much of the peak dynamics observed. To determine motif enrichments within each module, we calculate the fraction of motif instances in a given module peak set and divide by all motif instances in all observed peaks.

AML sample genotyping. All samples from the patients with AML described here were genotyped either by whole-exome sequencing using SeqCap EZ Exome SR kit v3.0 (Roche/NimbleGen) or by customized hybrid capture sequencing of the 130 genes most frequently mutated in AML[49] using the SeqCap EZ Choice kit (Roche/NimbleGen). Sequencing was performed on an Illumina HiSeq 2000, HiSeq 2500, or NextSeq 500 instrument. Sequence data were aligned to the hg19 human reference genome using BWA (v0.5.9) for global alignment and GATK (v2.8-1) for local realignment. Aligned reads were processed for downstream mutation calling using SAMtools (v0.1.12a). SNPs were called using GATK and Varscan (v2.3.7). All data derived from customized hybrid capture did not have a matched normal genome and were compared instead to the hg19 human reference genome. Putative SNPs were

filtered for (i) minimum sequence depth of 50 reads, (ii) less than 90% variant strand bias, (iii) nonsynonymous variants, (iv) a MAF less than 1%, if the SNP was observed in dbSNP, and (v) a minimum variant frequency of 5%. Indels were called using GATK[50] and Varscan[51]. Putative indels were filtered for (i) minimum sequence depth of 25, (ii) minimum variant frequency of 5%, (iii) less than 90% variant strand bias, and (iv) absence from dbSNP. Large-scale genomic events such as translocations were called using FACTERA[52] (v1.3) with no additional filtering. *FLT3* internal tandem duplications were called using Pindel[53] (v0.2.4) with no additional filtering. Manual observation was used to clarify borderline mutation calls. Additional weight was given to mutations called by more than one algorithm. All mutations were validated by targeted amplicon sequencing.

Targeted amplicon sequencing of leukemia-associated mutations. Targeted amplicon sequencing was performed as described previously[12].

Epigenetic variance calculation. Epigenetic variance was calculated as the sum of the squares of the distance from the mean divided by the number of samples. This is equivalent to the VAR.P function in Microsoft Excel. This variance was calculated for each individual peak. To obtain genome-wide variance, the rolling mean of 10,000 sequential peaks was calculated across the linear genome in chromosomal order. For calculations of epigenetic variance, some samples with high background were omitted.

Analysis of DNase data. DNase CD34 data, made available by the Epigenomics Roadmap Consortium, were downloaded from Sequence Read Archive (SRA) accessions SRR066150, SRR066151, SRR066152, SRR066351, SRR097542, SRR327476, and SRR327477. Single-end DNase data were aligned, filtered, and normalized using the methods described in ATAC-seq data analysis.

Correlating transcription factor motif deviation scores to expressed genes. Genes were first filtered for putative transcription factors ($n = 1,820$)[54]. $\log_2$ (fold change) and s.e.m. were computed using DESeq2. To determine robust correlation coefficients (Pearson) and P values for genes and transcription factor deviation scores, we permutated ($n = 1,000$) $\log_2$ (fold change) values according to the measurement error as determined by s.e.m. Reported Pearson correlation coefficients represent mean across for the sampled data. Reported P values represent a z-test statistic across the permutations.

To determine putative direct regulators of the given motif, we downloaded all available *in vitro* and inferred position weight matrices (PWMs) from CIS-BP[55]. We then calculated correlation coefficients (Pearson) for all CIS-BP PWMs ($n = 7,592$) with the unique set of hematopoiesis PWMs ($n = 46$). To account for offsets, we took the maximum calculated correlation coefficient after aligning two motifs in both orientations (reverse complement) and all possible offsets of length k. To filter the complete CIS-BP database ($n = 7,592$) to a non-redundant gene list ($n = 806$), we choose the motif with the maximum similarity (Pearson) to any hematopoiesis transcription factor motif (**Supplementary Fig. 9b** and **Supplementary Table 4**). To find putative direct regulators of human hematopoiesis, we filtered for transcription factors with a PWM correlation coefficient >0.8 (**Supplementary Fig. 9e**). Although we found that many transcription factors could be correlated with their motif usage, we report the most correlated transcription factor (**Supplementary Fig. 9g,h**) and the complete list in **Supplementary Table 4**.

Single-cell ATAC-seq analysis and enhancer cytometry. scATAC-seq and enhancer cytometry analysis were performed as described in the **Supplementary Note**.

Survival analysis. Overall survival was defined as the time from diagnosis to death from any cause. Relapse-free survival was defined as the time from complete morphological remission to the date of relapse of AML or death from any cause, whichever came first. Survival analysis was performed using the Kaplan–Meier estimate method. All patients were included for the analysis regardless of their treatment. P values comparing two Kaplan–Meier survival curves were calculated using the log-rank (Mantel–Cox) test. Hazard ratios were determined using the Mantel–Haenszel approach.

In vitro culture of primary AML cells for analysis of drug sensitivity. Primary AML blasts were cultured in Myelocult H5100 (Stemcell Technologies) with 20 ng/ml FLT3L, SCF, TPO, IL-3, and IL-6 and 0.5 μg/ml hydrocortisone. Blasts were cultured at 1 million cells/ml for a total of 6 d with no medium changes. Drug sensitivity was measured by flow cytometry analysis of Annexin V–negative, DAPI-negative live cells.

In vitro culture assays on HSPCs. FACS-purified HSPCs were plated into either myeloid differentiation medium (Myelocult H5100 with 20 ng/ml FLT3L, IL-3, TPO, SCF, and, GM-CSF and 0.5 μg/ml hydrocortisone) or erythroid differentiation medium (StemSpan SFEM II (Stemcell Technologies) with Erythroid Expansion Supplement (Stemcell Technologies)) and cultured for 6 d with medium changes as necessitated by cellular proliferation. Stemness retention medium was composed of HPGM (Lonza) containing 20 ng/ml FLT3L, SCF, and TPO.

Knockdown of *HOXA9*. *HOXA9* knockdown was achieved using the pRSI9 lentiviral backbone (Cellecta), which allows for constitutive expression of shRNA from a U6 promoter. The shRNA target sequences can be found in **Supplementary Table 7**.

Determination of half-maximal inhibitory concentration in primary AML cells. Cell death in response to pharmacological inhibition was measured by Annexin V staining using an Annexin V–Alexa Fluor 647 conjugate

(Life Technologies) according to the manufacturer's instructions. Responses were measured in relation to a vehicle-treated control.

46. Jan, M. *et al.* Prospective separation of normal and leukemic stem cells based on differential expression of TIM3, a human acute myeloid leukemia stem cell marker. *Proc. Natl. Acad. Sci. USA* **108**, 5009–5014 (2011).
47. Hansen, K.D., Irizarry, R.A. & Wu, Z. Removing technical variability in RNA-seq data using conditional quantile normalization. *Biostatistics* **13**, 204–216 (2012).
48. Buenrostro, J.D., Wu, B., Chang, H.Y. & Greenleaf, W.J. ATAC-seq: a method for assaying chromatin accessibility genome-wide. *Curr. Protoc. Mol. Biol.* **109**, 21.29.1–21.29.9 (2015).
49. Cancer Genome Atlas Research Network. Genomic and epigenomic landscapes of adult *de novo* acute myeloid leukemia. *N. Engl. J. Med.* **368**, 2059–2074 (2013).
50. McKenna, A. *et al.* The Genome Analysis Toolkit: a MapReduce framework for analyzing next-generation DNA sequencing data. *Genome Res.* **20**, 1297–1303 (2010).
51. Koboldt, D.C. *et al.* VarScan: variant detection in massively parallel sequencing of individual and pooled samples. *Bioinformatics* **25**, 2283–2285 (2009).
52. Newman, A.M. *et al.* FACTERA: a practical method for the discovery of genomic rearrangements at breakpoint resolution. *Bioinformatics* **30**, 3390–3393 (2014).
53. Ye, K., Schulz, M.H., Long, Q., Apweiler, R. & Ning, Z. Pindel: a pattern growth approach to detect break points of large deletions and medium sized insertions from paired-end short reads. *Bioinformatics* **25**, 2865–2871 (2009).
54. Vaquerizas, J.M., Kummerfeld, S.K., Teichmann, S.A. & Luscombe, N.M. A census of human transcription factors: function, expression and evolution. *Nat. Rev. Genet.* **10**, 252–263 (2009).
55. Weirauch, M.T. *et al.* Determination and inference of eukaryotic transcription factor sequence specificity. *Cell* **158**, 1431–1443 (2014).